Nano Research

Open Access

Research Article

Fabrication and application of porous organic single-crystal films in highly sensitive gas sensors

Zhangjin Chen[1], Suhui Wang[2], Mingke Yu[1], Peng Li[2], Xu Zhang[2], Hong Wang[1] ✉, Tengxiao Guo[2] ✉, and Chuan Liu[3] ✉

[1] *School of Materials, Shenzhen Campus of Sun Yat-sen University, Shenzhen 518107, China*
[2] *State Key Laboratory of NBC Protection for Civilian, Beijing 102205, China*
[3] *State Key Laboratory of Optoelectronic Materials and Technologies, Guangdong Province Key Laboratory of Display Material and Technology, School of Electronics and Information Technology, Sun Yat-sen University, Guangzhou 510006, China*

Cite this article: *Nano Research*, **2025**, *18*, 94907299. https://doi.org/10.26599/NR.2025.94907299

ABSTRACT: Gas sensors based on organic semiconductor materials (OSCs) have garnered significant attention due to their cost-effectiveness and ability to operate efficiently at room temperature. However, the performance of these sensors is often constrained by the grain boundaries and defects inherent in polycrystalline films typically produced by conventional methods. In this study, a novel approach was developed for fabricating large-area porous organic single-crystal films. Hydrophobic lattice structures were engineered on hydrophilic substrate surfaces, facilitating the growth of 2,7-dioctyl[1]benzothieno[3,2-b][1]benzothiophene (C8-BTBT) molecules by micro-spacing sublimation with liquid crystal properties. These hydrophobic lattice structures function as thermal stress release sites during the film cooling process, enabling the formation of organic single-crystal films with precisely controlled pore locations and sizes. The resulting porous films demonstrate electrical properties on stripes with those achieved through growing on bare silicon substrates, yet exhibit enhanced sensitivity, faster response times, and a lower detection limit when used as active layers in gas sensors. This technique offers a promising pathway for advancing high-performance organic gas sensors toward industrial application.

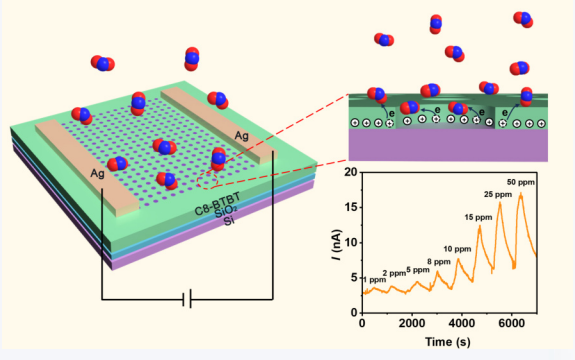

KEYWORDS: organic semiconductors, porous structures, organic single-crystals, gas sensors

1 Introduction

Gas sensors based on organic semiconductor materials (OSCs) have garnered significant attention due to their cost-effectiveness, low power consumption, and efficient operation at room temperature [1–5]. However, their performance is often constrained by the grain boundaries and defects inherent in polycrystalline films fabricated using conventional methods, which limit charge carrier mobility and introduce signal instability [6, 7]. Addressing these limitations is crucial for advancing OSC-based gas sensors, particularly in applications, such as environmental monitoring, industrial safety, and public health [8, 9].

Received: December 6, 2024; **Revised:** January 26, 2025
Accepted: February 8, 2025

✉Address correspondence to Hong Wang, wanghong3@mail.sysu.edu.cn; Tengxiao Guo, gtx23@qq.com; Chuan Liu, liuchuan5@mail.sysu.edu.cn

Single crystals, with their defect-free molecular structures, offer distinct advantages over polycrystalline materials for high-performance charge transport devices [10, 11]. The absence of grain boundaries and lattice defects significantly improves charge carrier mobility, enhancing device stability and response speed. These properties make single crystals ideal candidates for gas sensing applications [12–14]. However, in organic field-effect transistor (OFET)-based gas sensors, efficient diffusion of gas molecules to the semiconductor interface remains a significant challenge [15–17]. Strategies, such as reducing film thickness or introducing nanostructures, have been explored to enhance diffusion efficiency [18–21]. For instance, recent advancements have led to the development of various methods for preparing ultra-thin two-dimensional organic single-crystal thin films, such as solution shearing, spin coating, and solution epitaxy [22–24]. These ultra-thin structures significantly reduce the molecular diffusion distance, thereby markedly improving the sensitivity and response time of devices. However, these techniques often demand meticulous operational precision, and achieving consistent thickness remains a

challenge. In comparison, vapor deposition provides a sampler and more controllable approach, offering greater ease of operation and more reliable thickness control.

Introducing porous structures into OSC films has proven effective in addressing diffusion limitations by increasing the surface area available for gas interactions while maintaining charge transport efficiency [25–27]. However, existing porous structures are typically based on amorphous or polycrystalline films, which exhibit suboptimal electrical performance [28–31]. Notably, Li et al. demonstrated that incorporating porous single-crystal films into OFET sensors enabled a detection limit as low as 0.1 ppb for NH_3. This significant performance improvement underscores the potential of porous single-crystal films [32]. However, their fabrication method—drop-casting yields films with poorly controlled pore size and distribution, limiting their practical applicability. Overcoming these limitations is essential for the broader adoption of such structures in high-performance gas sensors.

This study addresses these challenges by developing a novel method for fabricating large-area organic porous single-crystal films with precise control over molecular layer thickness, pore size, density, and spatial distribution. Leveraging the liquid crystalline properties of OSC molecules, films are grown on hydrophilic substrates pre-patterned with hydrophobic lattice structures, which act as thermal stress release sites during the cooling process. This approach ensures controlled pore characteristics while maintaining the single-crystal quality of the films. Gas sensors utilizing these films demonstrate enhanced sensitivity, faster response times, and a lower detection limit compared to non-porous counterparts. Furthermore, the scalability and reproducibility of this method pave the way for industrial applications, providing a promising pathway for advancing high-performance organic gas sensors.

2 Results and discussion

2.1 Preparation and characterization of thin films

In this study, 2,7-dioctyl[1]benzothieno[3,2-b][1]benzothiophene (C8-BTBT, molecular structure is shown in Fig. S1 in the Electronic Supplementary Material (ESM)) was selected due to its prominent application as an organic semiconductor material in organic electronics, owing to its superior crystallization properties and high charge carrier mobility [33, 34]. Notably, C8-BTBT is a liquid crystal material with a melting point of 109 °C and maintains a liquid crystalline phase between 109 and 125 °C [35]. This characteristic allows for controlled crystallization within this temperature range, facilitating precise adjustment of the material's crystalline properties during the intermediate phase. Figure 1(a) illustrates the fabrication process of the porous organic film. First, electron beam lithography (EBL) was employed to create a porous structure on a polymethyl methacrylate (PMMA) resist layer coated on a silicon wafer substrate, exposing the SiO_2 surface. Octadecyltrichlorosilane (OTS) was then used to chemically modify the exposed SiO_2 surface, forming a hydrophobic OTS-patterned array after the PMMA resist was removed. Subsequently, micro-spacing in-air sublimation was used to grow C8-BTBT molecules on the sample surface [36]. Specifically, the sample was inverted over a silicon wafer coated with C8-BTBT molecules, with the OTS-patterned side facing the C8-BTBT source, and a 120 μm-thick glass spacer placed between them. The sample was heated on a hotplate preheated to 200 °C for 30 s, resulting in the growth of a porous single-crystal C8-BTBT film on the substrate surface.

The growth of C8-BTBT using micro-spacing in-air sublimation has been previously documented [37, 38]. Compared to vacuum evaporation, C8-BTBT exhibits a higher surface tension when it forms a melt in the atmosphere at temperatures exceeding its gas-phase melting point, facilitating its spreading and film formation on the substrate. This property enables the fabrication of large-area thin film structures. However, the obtained films often exhibit cracking after growth. As illustrated in Fig. 1(b), a crystalline film grown at 200 °C for 30 s exhibits stripe-like patterns with numerous nearly parallel but randomly oriented cracks. The inset shows a high-resolution scanning electron microscopy (SEM) image of the stripes. Although the stripe orientation is consistent, the widths vary. This phenomenon, also reported in the literature, is associated with the phase transition of C8-BTBT from liquid to solid during cooling [37]. The resulting thermal mismatch between the material and substrate causes volume contraction and generates cracks. On a smaller scale, the cracks are orderly, but on larger scales, they extend in various random directions (Fig. S2 in the ESM). For high-

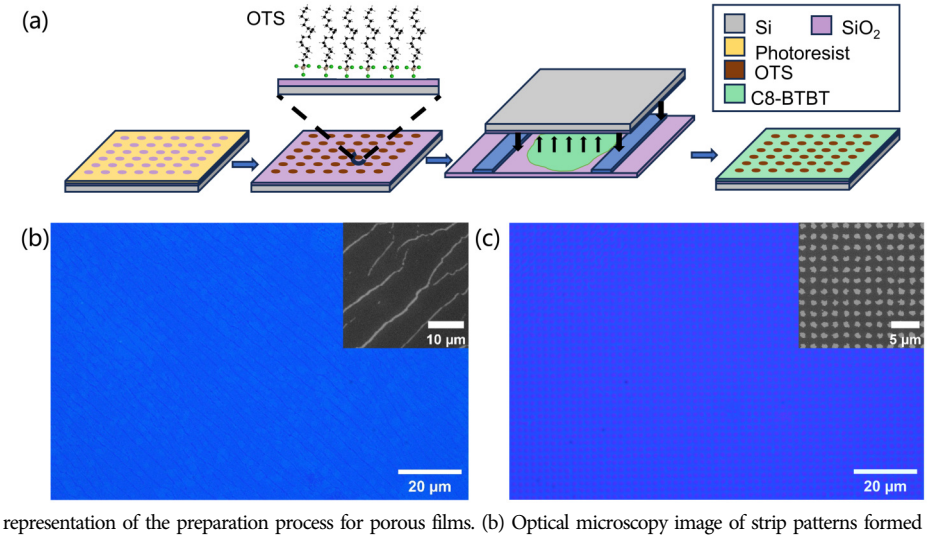

Figure 1 (a) Schematic representation of the preparation process for porous films. (b) Optical microscopy image of strip patterns formed on a bare SiO_2 surface. (c) Optical microscopy image of a porous film with a pore size and spacing of 1.0 μm, fabricated on a SiO_2 surface patterned with OTS dot arrays. The insets in (b) and (c) present the corresponding high-resolution SEM images, highlighting the detailed microstructures of the films.

performance device fabrication, it is crucial to align source–drain electrodes with the direction of these cracks to facilitate uninterrupted carrier transport in the channel, which poses significant challenges for scaling up the production of high-performance OFETs. To address this issue, a sparse crystal lattice structure was introduced on the substrate surface to serve as thermal stress release points. This approach facilitated the formation of the organic porous structure is depicted in Fig. 1(c), with a high-resolution SEM image of the film shown in the inset, and effectively mitigating the cracking typically observed during direct growth. As shown in Fig. S3 in the ESM, a large-area optical microscopy image confirms that the porous film structure remains intact across the entire region with the OTS lattice. The formation of the porous structure is attributed to the hydrophobic nature of OTS-modified silica surfaces. The methyl ($-CH_3$) groups at the ends of OTS molecules are nonpolar and exhibit weak interactions with C8-BTBT molecules, making adsorption in these regions difficult. This weak interaction increases the mobility and desorption likelihood of C8-BTBT molecules on the surface, hindering the formation of stable nucleation centers. As a result, nucleation and film growth occur primarily in the hydrophilic regions.

This method not only mitigates crack formation in large-area films but also allows for precise control over the size and density of the pores by adjusting the dimensions and spacing of the OTS dots. Lattices with OTS patterns of 0.8, 1.0, 1.2, and 1.5 μm diameters, with spacing corresponding to the dot diameters, were fabricated. Crystalline films were subsequently grown at 200 °C for 30 s. Optical microscopy characterization of the large-area films, as shown in Figs. 2(a)–2(d), reveals a uniform grid-like structure with consistent coloration across the grid, indicating uniform film thickness. The pore sizes within the grid increase progressively with the diameter of the OTS dots. In addition, the thickness of the film can be precisely controlled by adjusting the growth parameters. For instance, increasing the growth time from 30 to 120 s when the temperature was set as 190 °C resulted in an increase in the thickness of the porous film from 5.6 to 26.2 nm (see Fig. S4 in the ESM). The large-scale uniformity of the film is achieved by ensuring the uniform dispersion of the C8-BTBT source across the underlying silicon wafer [37].

Further surface characterization was conducted using atomic force microscopy (AFM). Figure 2(e) presents the AFM image of the OTS pattern with a diameter of 0.8 μm, revealing a uniform grid-like structure with minimal defects and no visible cracks. An enlarged view of a specific region, shown in the inset, highlights approximately circular pores that closely align with the intended dimensions. As the pore size increases, the AFM images in Figs. 2(f)–2(h) display structures similar to the 0.8 μm OTS pattern, indicating that the designed OTS hydrophobic lattice effectively suppresses crack formation in C8-BTBT films within a specific size range. This enables the fabrication of organic single-crystal thin films with tunable pore sizes and densities. Although the pattern sizes investigated in this study were limited to 0.8–1.5 μm, it is hypothesized that similar control could be achieved with smaller sizes. However, this could not be verified due to the resolution limitations of the EBL system employed. On the other hand, increasing the pattern size beyond 1.5 μm compromises control over crack confinement. At 1.8 μm, minor defects begin to appear, while at 2.0 μm, a significant increase in defects occurs, leading to the loss of effective crack control (see Fig. S5 in the ESM).

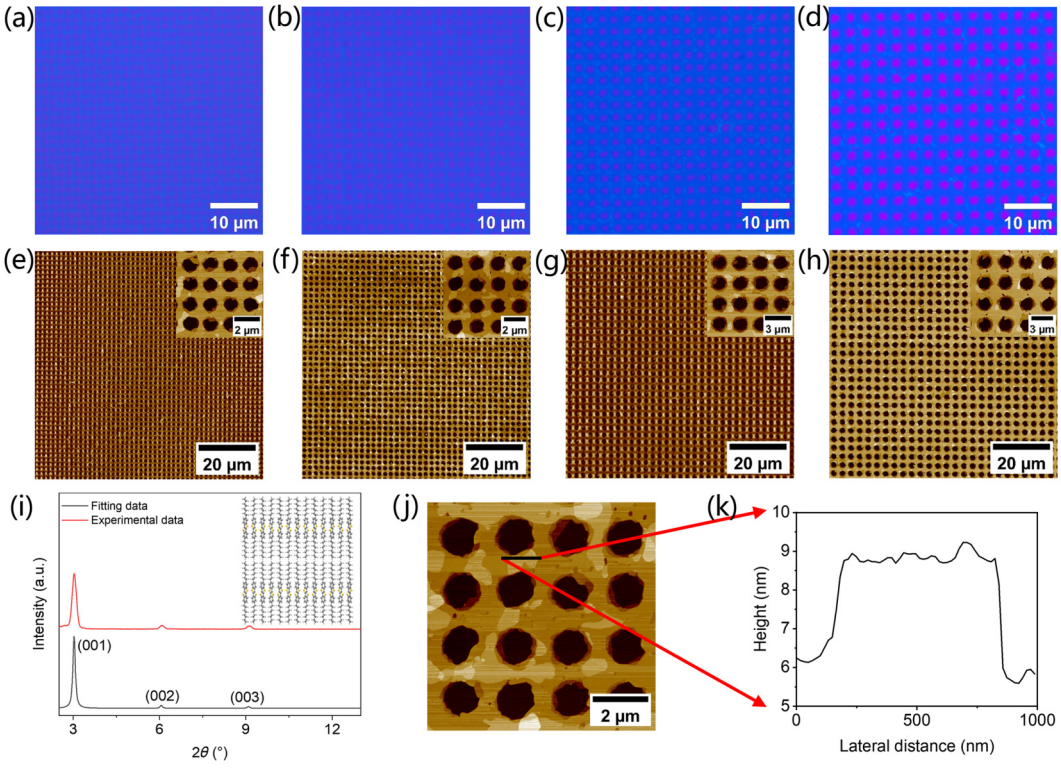

Figure 2 ((a)–(d)) Optical microscopy images of porous thin films with pore sizes and spacings of 0.8, 1.0, 1.2, and 1.5 μm. ((e)–(h)) AFM images of the corresponding samples in ((a)–(d)), with insets showing high-resolution views of the samples. (i) XRD patterns of the C8-BTBT porous film. The inset provides a schematic representation of the molecular arrangement of C8-BTBT within the film. (j) High-resolution AFM image of the C8-BTBT porous film with a pore size of 1.0 μm. (k) Cross-sectional profile of the sample along the black line segments indicated in (j).

To ascertain the single-crystal properties of the fabricated films, a series of characterization techniques were employed. As illustrated in Fig. S6 in the ESM, SEM images demonstrate that the film remains intact and continuous within the porous lattice. The pores exhibit a well-defined morphology, with sizes and spacing closely aligned with the designed pattern and no observable cracks. This demonstrates the effectiveness of the pore structure in mitigating crack formation. As illustrated in Fig. 2(i), the X-ray diffraction (XRD) patterns of the porous single-crystal film exhibit three distinct and sharp diffraction peaks at 3.03°, 6.05°, and 9.13°. These peaks correspond to the (001), (002), and (003) planes, consistent with the fitted XRD patterns of C8-BTBT single crystals [39, 40]. The presence of these peaks confirms the film's high crystallinity and indicates that the C8-BTBT molecules adopt a layered arrangement along the *c*-axis, perpendicular to the substrate. This molecular arrangement is illustrated in the inset of Fig. 2(i). Figure 2(j) illustrates the results of high-resolution AFM measurement, which reveals prominent step-flow structural features on the film surface. The cross-sectional profile along the black line, depicted in Fig. 2(k), distinctly shows a step structure. Statistical analysis indicates a step height of 3.03 ± 0.06 nm, which matches the thickness of a single C8-BTBT molecular layer. This observation suggests a sub-monolayer molecular coverage on the top surface of the porous film. Considering the absence of obvious domain boundaries in previously acquired large-scale AFM images, the observed structure can be confidently identified as a porous single-crystal thin film. It is worth noting that small concave structures observed in the high-resolution AFM images are defects resulting from an excessively rapid growth rate. By reducing the growth rate, these defects can largely be eliminated.

Additionally, polarized optical microscopy characterization was performed on the samples (Fig. S7 in the ESM). The porous film exhibited uniform color changes and extinction behavior as the polarizer was rotated. In contrast, the film grown in areas without the hydrophobic lattice showed inconsistent color changes, indicating random crystalline orientations. This further confirms that the continuity of the porous film results in uniform molecular alignment, leading to consistent crystal orientation across the entire film. The formation of this structure is attributed to the liquid crystal properties of C8-BTBT. During the transition from the liquid crystal state to the crystalline state, the intact liquid crystal phase facilitates the formation of a well-ordered crystal structure with uniform internal molecular arrangement and orientation [38].

The mechanism by which the sparse crystal lattice structure reduces thermal stress and prevents cracking in single-crystal thin films was analyzed based on experimental observations. In this study, single-crystal thin films of C8-BTBT were grown at a temperature of 200 °C. During the cooling process, the films underwent a phase transition from a liquid state to a liquid-crystalline state and subsequently to a solid state, accompanied by notable changes in density. Due to the significant disparity in thermal expansion coefficients between the C8-BTBT film and the SiO_2 substrate, thermal stress is generated during the cooling process. To investigate this phenomenon, a thermal stress distribution simulation was conducted using COMSOL Multiphysics.

In the simulation, a 1 μm-thick film was modeled on a rectangular prism substrate with dimensions of 50 μm × 50 μm × 5 μm. The thermal expansion coefficient of the film was set at a value higher than that of the substrate, and the material properties were assumed to be isotropic. The distribution of steady-state thermal stress after cooling was calculated. As illustrated in Fig. 3(a), substantial thermal stress was evident within the film, with the stress concentration occurring in the vicinity of the film's center. However, the stress magnitude along the edges of the substrate remained uniform. On a bare silicon substrate, this stress distribution results in film splitting along the *b*-axis direction, where intermolecular interactions are weakest, leading to the formation of a striped morphology [37, 40].

The introduction of a hydrophobic lattice structure onto the substrate surface, as illustrated in Fig. 3(b), effectively alleviates internal stress within the film by redistributing it around the lattice dots. The localized stress concentrations exceed the maximum stress experienced by the bare substrate, promoting the release of thermal stress through molecular mobility. This results in localized slippage of the film around the OTS dots, dissipating the accumulated stress energy. The stress relaxation is evidenced by the irregular morphology surrounding the holes. High-resolution AFM image of specific holes reveals distinct layered structures, further supporting the proposed stress-relief mechanism. This mechanism helps maintain the film's structural integrity, as the hydrophobic lattice structure mitigates thermal stress and prevents crack formation in single-crystal thin films. However, it is important to note that the introduction of this porous structure does not improve the mechanical properties of the film (see Fig. S8 in the ESM).

At the microscopic level, as shown in Fig. 3(c), the transition from the liquid-crystalline to the crystalline phase entails a shift from a structure with long-range order and short-range disorder to a fully ordered arrangement, which necessitates molecular rearrangement [41]. This phase change is accompanied by a substantial volume contraction, which causes the film to contract

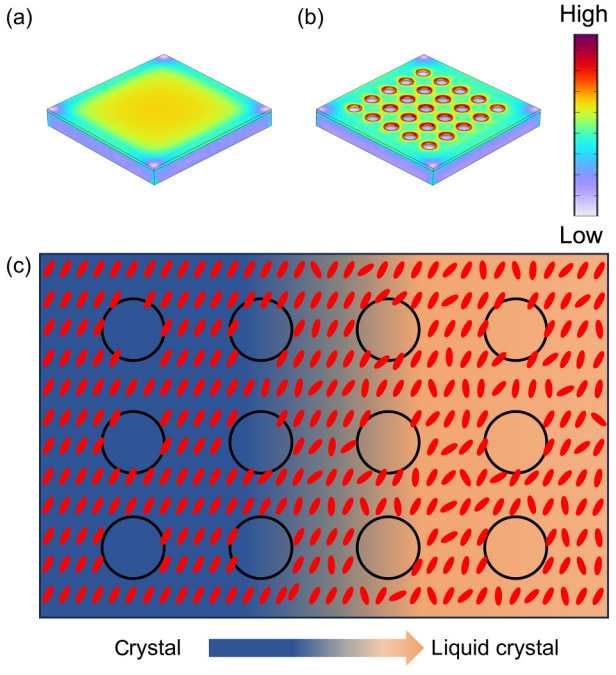

Figure 3 ((a) and (b)) Schematic illustration of the thermal stress release mechanism in C8-BTBT single-crystal thin films (a) without and (b) with an OTS hydrophobic lattice structure. (c) Schematic representation of molecular arrangement and diffusion dynamics during the transition from the liquid crystal phase to the crystalline phase.

and crack along directions with the weakest intermolecular interactions. The spacing of these cracks is dependent upon the average free molecular path on the substrate surface and the degree of volume contraction in the film [42]. A statistical analysis of multiple film samples indicates an average crack spacing of approximately 2.0 μm (Fig. S9 in the ESM). The introduction of a hydrophobic lattice enables C8-BTBT molecules to diffuse into lattice regions, effectively filling potential crack sites and preventing film rupture. In order to achieve optimal crack suppression, it is necessary that the lattice spacing be less than or equal to the average crack spacing. In accordance with prior observations, the effectiveness of this approach is significantly diminished when the lattice spacing exceeds 1.8 μm, and once it surpasses 2 μm, the method becomes almost entirely ineffective. This serves to highlight the critical role of lattice spacing in maintaining the structural integrity of single-crystal films. Notably, based on the growth mechanism of porous single-crystal thin films, this method theoretically enables the growth of organic single-crystal thin films on scales ranging from large areas to wafer sizes.

2.2 Device fabrication and electrical performance characterization

Bottom-gate, top-contact OFET devices were fabricated by depositing Ag electrodes onto porous single-crystal C8-BTBT thin films. A schematic of the device structure is presented in Fig. 4(a), with the pore size and spacing in the film set at 1 μm. A SEM image of the fabricated OFET device is shown in Fig. S10 in the ESM. The device features an effective channel width of 75 μm and a channel length of 45 μm. The conductivity of the device, determined through current–voltage (I–V, where I is the source–drain current and V is the source–drain voltage of the OFET) measurements, was calculated to be 1.19×10^{-3} S·m^{-1} (see Fig. S11 in the ESM). Due to its p-type semiconductor characteristics, C8-BTBT facilitates the generation of additional hole carriers at the interface between the channel and the dielectric layer upon the application of a negative gate voltage, significantly enhancing the device's current conduction capability. Figures 4(b) and 4(c) illustrate the output and transfer characteristics of the device, exhibiting typical p-type behavior. The mobility reliability factor of the device was calculated to be 0.71. Statistical analysis of 28 device samples, as depicted in the histogram in Fig. 4(d), reveals an average saturation mobility of 2.40 cm^2·V^{-1}·s^{-1} and a maximum mobility of 5.16 cm^2·V^{-1}·s^{-1}. The minimal variability in device performance highlights the stability and uniformity of the fabrication process. Furthermore, the mobility achieved with films prepared using other OTS lattice sizes is comparable to that obtained with the 1 μm lattice size (Fig. S12 in the ESM).

For comparison, OFET devices were also fabricated on stripe-patterned C8-BTBT films grown under identical conditions on bare silicon substrates. The results, shown in Fig. S13 in the ESM, indicate an average saturation mobility of 3.98 cm^2·V^{-1}·s^{-1} and a maximum mobility of 7.72 cm^2·V^{-1}·s^{-1}. Despite the intentional introduction of pores as structural features, the single-crystal nature

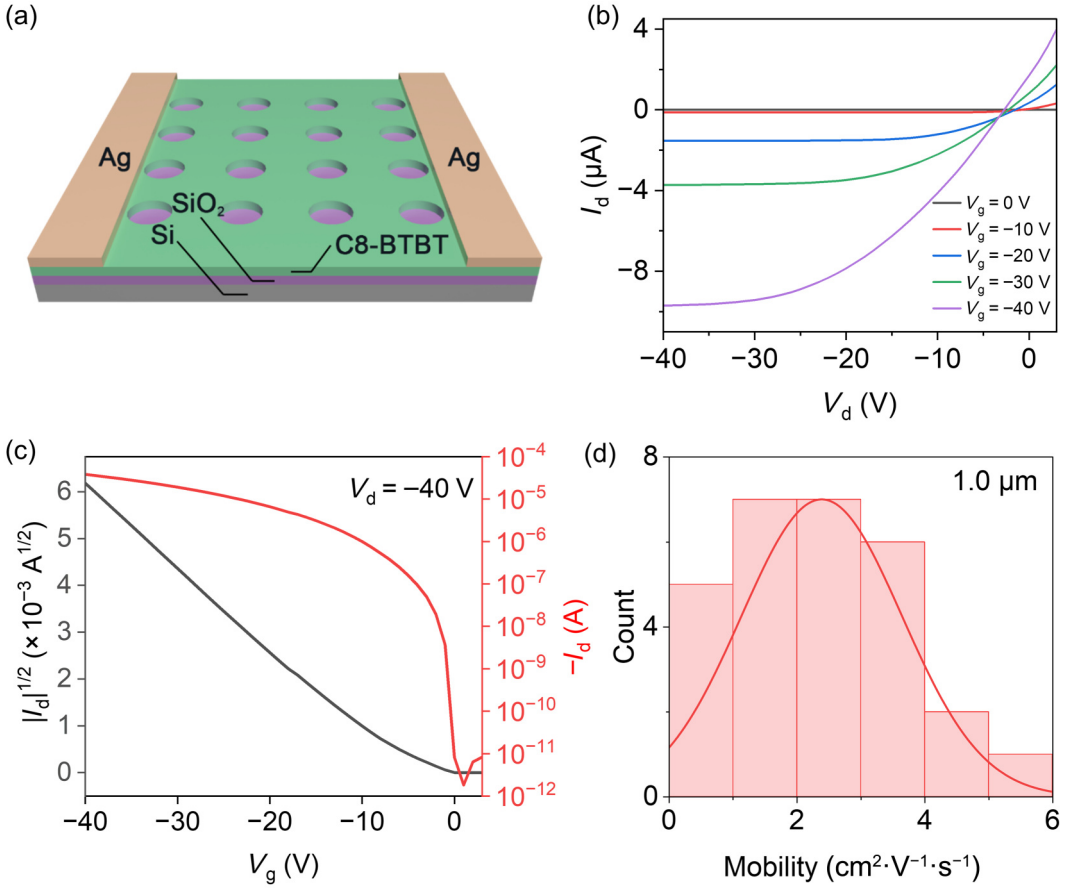

Figure 4 (a) Schematic illustration of the OFET device structure with a bottom-gate, top-contact configuration utilizing a C8-BTBT porous organic single-crystal film. (b) Output characteristics and (c) transfer characteristics of a representative OFET device. (d) Histogram showing the distribution of charge carrier mobility values for the OFET devices, calculated in the saturation region.

of the film, characterized by long-range molecular order and uniform thickness, ensures that carrier mobility remains largely unaffected. These findings demonstrate that the presence of pores does not significantly compromise device performance, which remains at a high level.

2.3 Gas sensing performance

The device, fabricated using a strategy involving porous films, is suitable for direct application in gas detection. To evaluate the gas-sensing performance, devices were placed in a gas test chamber with pure N_2 serving as the background gas. Oxidizing gas (NO_2) and reducing gas (NH_3) were selected as test gases. C8-BTBT exhibits significant selective adsorption capabilities for NO_2 and NH_3, even in the presence of N_2 (Fig. S14 in the ESM). To evaluate the device's response, various concentrations of these test gases were prepared by mixing them with nitrogen at different ratios and were periodically introduced into the test chamber. The gas flow rates for NO_2 and N_2 were controlled by a computer, with flow durations set to 4 min for NO_2 and 10 min for N_2, respectively.

Figure 5(a) depicts the comparative current response ($\Delta I/I_0 \times 100\%$) of multiple devices subjected to varying concentrations of NO_2. Here, I_0 defined as the baseline source–drain current measured under a controlled N_2 atmosphere prior to gas exposure. ΔI is calculated as the difference between the post-exposure source–drain current measured upon introduction of the target gas at a specified concentration and the initial baseline current I_0. At a concentration of 1 ppm, the devices exhibited an average relative response of 31.19%. The response increased with higher NO_2 concentrations, but it began to plateau beyond 15 ppm, indicating a saturation effect (Fig. S15 in the ESM). At a concentration of 50 ppm, the devices exhibited an average relative response of 668.62%. Within the linear response range of 1–15 ppm, the sensitivity was calculated to be 25.01 %·ppm^{-1}. Figure 5(b) illustrates the dynamic response curve of the porous film devices under a 500 mL·min^{-1} flow rate, which demonstrates a clear increase in current with rising NO_2 concentrations. The limit of detection (LOD) was determined using the signal-to-noise ratio (SNR) method (SNR = 3), yielding a value of 2.14 ppb. This result demonstrates the high sensitivity of the porous film devices.

For purposes of comparison, stripe-patterned devices were also evaluated under identical conditions, as illustrated in Fig. S16 in the ESM. The devices demonstrated a comparable linear response within the 1–15 ppm range; however, they exhibited a reduced sensitivity of 22.37 %·ppm^{-1} and an elevated LOD of 3.57 ppb. Notwithstanding their elevated baseline current under identical applied voltage, the stripe-patterned devices demonstrated reduced responsiveness. With regard to the kinetics of the response, Fig. S15 in the ESM indicates that the porous film devices exhibited a response time of 108 s and a recovery time of 374 s for NO_2. In contrast, the stripe-patterned devices exhibited longer response and recovery times, with values of 114 and 502 s, respectively. These findings underscore the enhanced sensitivity and accelerated response of porous film devices in comparison to their stripe-patterned counterparts.

Figure 5(d) demonstrates the negative relative response of the device to NH_3, with a response of −7.94% observed at a concentration of 1 ppm. The response increases proportionally with NH_3 concentration but begins to plateau beyond 5 ppm. At 50 ppm, the device achieves a relative response of −68.80% (Fig. S17 in the ESM). Within the linear response range of 1–5 ppm, the sensitivity was determined to be −5.12 %·ppm^{-1}, and the limit of detection, calculated using the SNR method (SNR = 3), was 18.10 ppb. The dynamic response curve of the porous film device to varying NH_3 concentrations is shown in Fig. 5(e), indicating consistent response behavior with increasing concentrations. For comparison, stripe-patterned film devices exhibited a similar response trend but with a lower average relative response compared to the porous film devices, as shown in Fig. S18 in the ESM. These stripe-patterned devices showed a sensitivity of −4.31 %·ppm^{-1} and an LOD of 19.30 ppb. In terms of response kinetics, the porous film device demonstrated a response time of 83 s and a recovery time of

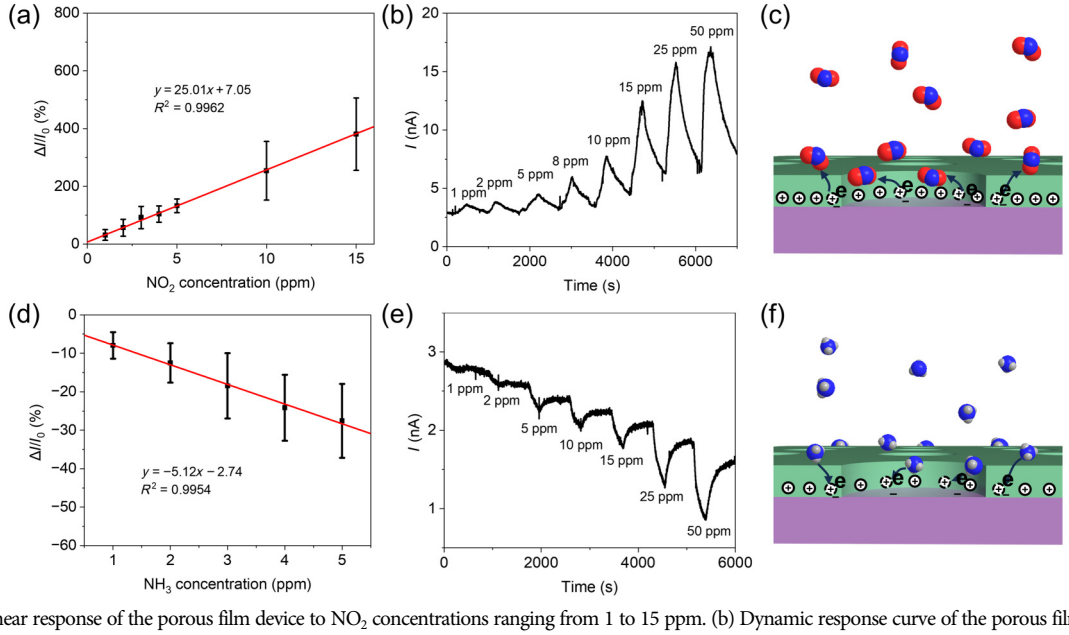

Figure 5 (a) Linear response of the porous film device to NO_2 concentrations ranging from 1 to 15 ppm. (b) Dynamic response curve of the porous film device to NO_2. (c) Schematic representation of the working mechanism of the porous single-crystal structure during NO_2 sensing. (d) Linear response of the device to NH_3 concentrations ranging from 1 to 5 ppm. (e) Dynamic response curve of the porous film device to NH_3. (f) Schematic representation of the working mechanism of the porous single-crystal structure during NH_3 sensing. The error bars represent standard deviations of measurements.

115 s (Fig. S17 in the ESM). In contrast, the stripe-patterned device had a slightly longer response time of 96 s and showed incomplete recovery to the baseline after stabilization, with an extended recovery time of 121 s.

The operating mechanism of organic semiconductor devices involves the interaction between the oxidizing gas NO_2 and the C8-BTBT film. Upon contact, NO_2 molecules are physically adsorbed onto the surface of the film and diffuse into the active layer of the organic semiconductor. Due to its strong oxidizing ability, NO_2 captures electrons from the C8-BTBT molecules upon adsorption, leading to an increase in hole concentration in the channel. This enhances the conductivity of the p-type semiconductor, resulting in an increase in current. As shown in Fig. 5(c), the porous structure significantly enlarges the contact area between the gas and the C8-BTBT active layer, facilitating the diffusion of gas molecules into the thin film. Moreover, the interconnected pores allow for more direct interactions between the gas molecules and the charge carriers in the conductive channel, lowering diffusion barriers, and accelerating both adsorption and desorption processes. Consequently, the porous structure results in higher detection current and faster response/recovery speed compared to the stripe-patterned devices. Similarly, the sensing mechanism for NH_3, as illustrated in Fig. 5(f), operates on a comparable principle but with an inverse effect. As a reducing gas, NH_3 donates electrons to the semiconductor layer, which reduces the hole concentration at the interface and consequently decreases the detection current. Despite the molecules being adsorbed onto the substrate surface through weak van der Waals forces, the strong π–π interactions within the C8-BTBT crystal impart excellent stability to the porous film. As a result, the device demonstrates robust stability, retaining 86% of its initial performance even after exposure to atmospheric conditions for six months (Fig. S19 in the ESM). The device's anti-humidity performance was evaluated under varying humidity conditions (Fig. S20 in the ESM). The results demonstrated a significant reduction in sensitivity to NO_2, while the sensitivity to NH_3 was enhanced. This behavior can be attributed to the impact of water vapor on the adsorption of different gases and the modulation of charge carrier density [43, 44].

The preparation of porous single-crystal structures offers distinct advantages over stripe-patterned thin-film structures, including faster response and recovery times, enhanced sensitivity, and lower detection limits. While the gas-sensing performance of the devices in this study may not be among the highest reported, this limitation primarily arises from the inherent gas-response characteristics of C8-BTBT. Sensitivity can be significantly enhanced by operating the device in an OFET configuration with negative gate voltages. The modulation of the gate voltage further amplifies the change in charge carrier density induced by the gas, leading to a gas response to NO_2 and NH_3 that is 3.5 and 2.0 times greater, respectively, compared to a resistive device (Fig. S21 in the ESM). Future improvements could focus on synthesizing alternative organic semiconductor molecules with enhanced gas-sensing properties or integrating functional molecules into the films to further boost their performance [45, 46]. Compared to other commonly used gas sensors, the device developed in this study meets the performance benchmarks for practical application (see Table S1 in the ESM). Additionally, it offers key advantages, such as low operating temperature, cost-effectiveness, and ease of operation, presenting significant potential for real-world applications. Moreover, the compatibility of this approach with photolithography, coupled with its precise control over film thickness, hole size, and distribution, underscores its strong potential for industrial-scale applications.

3 Conclusions

In summary, a method for fabricating large-scale porous organic single-crystal films has been developed by implementing hydrophobic lattice structures on hydrophilic substrates. This design serves as stress release points to address the film rupture that typically arises due to mismatched thermal expansion coefficients between the substrate and liquid crystal material during cooling. This approach effectively achieves precise and controllable pore sizes and positions in the porous single-crystal films, which can then function as the active layer in gas sensors, enhancing the device's sensitivity and response rate. The strategy provides a robust foundation for advancing high-performance organic gas sensors and paves the way for applications in industrial settings.

4 Experimental

4.1 Materials

C8-BTBT was procured from Derthon Optoelectronic Materials Science Co., Ltd. and used without further purification. Silicon wafers with a 300 nm thermal oxide layer were obtained from Sunson Electronics. PMMA (950 A4) for photolithography was purchased from Beijing Boning Biotechnology Co., Ltd.

4.2 Film preparation

PMMA photoresist was spin-coated onto a clean silicon wafer at 4000 rpm for 45 s, followed by baking on a hotplate at 180 °C for 60 s. A pattern of holes was created on the photoresist using electron beam lithography, with hole size and spacing precisely controlled via computer. The wafer was then immersed in a developer solution of methyl isobutyl ketone (MIBK) and isopropyl alcohol (IPA) (1:3 ratio) to form the patterned array. Hydrophobic silane OTS was employed to modify the patterned areas of the substrate in a vacuum environment at 120 °C, forming a hydrophobic monolayer. After stripping the photoresist and cleaning the substrate, the sample with a patterned hydrophobic array was prepared. This substrate was then inverted above a second substrate coated with organic semiconductor liquid crystal molecules, separated by a micrometer-scale spacer. Heating the substrates facilitated the vaporization of the organic semiconductor liquid crystal molecules, which then condensed onto the substrate, resulting in the formation of the organic porous single-crystal film.

4.3 Film characterization

The surface morphology of the films was characterized using AFM measurement with a Horiba Smart SPM. SEM images were captured with a Hitachi SU 5000 at an accelerating voltage of 5 kV. XRD measurements were performed using a Malvern PANalytical Empyream system.

4.4 COMSOL simulation

Simulation was performed at the steady state using the solid mechanics module. A 1 μm-thick film was simulated on a rectangular prism substrate with dimensions of 50 μm × 50 μm × 5 μm. The thermal expansion coefficient of the film was assigned a value greater than that of the substrate, with both materials assumed to exhibit isotropic properties. The initial temperature of

the substrate and film was set to 120 °C, and the final temperature was set to room temperature of 25 °C. The remaining parameters were set to the system default values.

4.5 Device fabrication and characterization

Silver electrodes (100 nm) were deposited onto the films using a mask in a vacuum environment to fabricate bottom-gate, top-contact organic field-effect transistor devices, with both channel length and width set to 100 μm. Device performance was evaluated using a Keithley 4200-SCS. For gas sensing tests, the devices were placed in a sealed polytetrafluoroethylene (PTFE) chamber, with gases introduced through tubing. The chemical resistance and performance response of the devices under various gas environments were measured using a Keithley 2400.

Electronic Supplementary Material: Supplementary material (further details of the molecular structure, optical microscopy, AFM images, SEM images, polarized light microscopy, electrical performance characterization curves, and gas response results of devices based on porous single-crystal thin films and striped structures) is available in the online version of this article at https://doi.org/10.26599/NR.2025.94907299.

Data availability

All data needed to support the conclusions in the paper are presented in the manuscript and the Electronic Supplementary Material. Additional data related to this paper may be requested from the corresponding author upon request.

Acknowledgements

The authors are grateful to the financial support from the Shenzhen Science and Technology Program (No. JCYJ20220530150210023), Scientific Research Fund of the State Key Laboratory of NBC Protection for Civilian (No. SKLNBC2019-2), and Guangdong Basic and Applied Basic Research Foundation (No. 2021A1515110620).

Declaration of competing interest

All the contributing authors report no conflict of interests in this work.

Author contribution statement

Z. J. C.: Investigation, conceptualization, data curation, formal analysis, methodology, visualization, writing – original draft. S. H. W.: Data curation, formal analysis, software, conceptualization, writing – original draft. M. K. Y.: Data curation, conceptualization, software. P. L.: Formal analysis, methodology. X. Z.: Methodology. H. W.: Resources, supervision, formal analysis, writing – review & editing, project administration, funding acquisition. T. X. G.: Supervision, writing – review & editing, project administration, funding acquisition. C. L.: Supervision, resources, writing – review & editing, project administration. All the authors have approved the final manuscript.

Use of AI statement

None.

References

[1] Zhou, S. X.; Zhao, Y. J.; Xun, Y. R.; Wei, Z. C.; Yang, Y.; Yan, W. T.; Ding, J. Programmable and modularized gas sensor integrated by 3D printing. *Chem. Rev.* **2024**, *124*, 3608–3643.

[2] Mo, X. C.; Zhu, C. H.; Zhang, Z. R.; Yan, X. H.; Han, C. S.; Li, J. X.; Attfield, J. P.; Yang, M. H. Nitrogen-doped indium oxide electrochemical sensor for stable and selective NO_2 detection. *Adv. Mater.* **2024**, *36*, 2409294.

[3] Wang, Q.; Wang, M. L.; Zheng, K. P.; Ye, W. N.; Zhang, S.; Wang, B. B.; Long, X. J. High-performance room temperature ammonia sensors based on pure organic molecules featuring B–N covalent bond. *Adv. Sci.* **2024**, *11*, 2308483.

[4] Rajeev, G.; Prieto Simon, B.; Marsal, L. F.; Voelcker, N. H. Advances in nanoporous anodic alumina-based biosensors to detect biomarkers of clinical significance: A review. *Adv. Healthcare Mater.* **2018**, *7*, 1700904.

[5] Wang, Z.; Huang, L. Z.; Zhu, X. F.; Zhou, X.; Chi, L. F. An ultrasensitive organic semiconductor NO_2 sensor based on crystalline TIPS-pentacene films. *Adv. Mater.* **2017**, *29*, 1703192.

[6] Bangsund, J. S.; Fielitz, T. R.; Steiner, T. J.; Shi, K. C.; Van Sambeek, J. R.; Clark, C. P.; Holmes, R. J. Formation of aligned periodic patterns during the crystallization of organic semiconductor thin films. *Nat. Mater.* **2019**, *18*, 725–731.

[7] Kim, K.; Bae, J.; Noh, S. H.; Jang, J.; Kim, S. H.; Park, C. E. Direct writing and aligning of small-molecule organic semiconductor crystals via "dragging mode" electrohydrodynamic jet printing for flexible organic field-effect transistor arrays. *J. Phys. Chem. Lett.* **2017**, *8*, 5492–5500.

[8] Atkinson, J. T.; Su, L.; Zhang, X.; Bennett, G. N.; Silberg, J. J.; Ajo-Franklin, C. M. Real-time bioelectronic sensing of environmental contaminants. *Nature* **2022**, *611*, 548–553.

[9] Lin, P.; Yan, F. Organic thin-film transistors for chemical and biological sensing. *Adv. Mater.* **2012**, *24*, 34–51.

[10] Deng, W.; Lei, H. M.; Zhang, X. J.; Sheng, F. M.; Shi, J. L.; Zhang, X. L.; Liu, X. Y.; Grigorian, S.; Zhang, X. H.; Jie, J. S. Scalable growth of organic single-crystal films via an orientation filter funnel for high-performance transistors with excellent uniformity. *Adv. Mater.* **2022**, *34*, 2109818.

[11] Zhang, X. T.; Dong, H. L.; Hu, W. P. Organic semiconductor single crystals for electronics and photonics. *Adv. Mater.* **2018**, *30*, 1801048.

[12] Chen, Z.; Duan, S. M.; Zhang, X. T.; Geng, B. W.; Xiao, Y. L.; Jie, J. S.; Dong, H. L.; Li, L. Q.; Hu, W. P. Organic semiconductor crystal engineering for high-resolution layer-controlled 2D crystal arrays. *Adv. Mater.* **2022**, *34*, 2104166.

[13] Cavallari, M. R.; Pastrana, L. M.; Sosa, C. D. F.; Marquina, A. M. R.; Izquierdo, J. E. E.; Fonseca, F. J.; de Amorim, C. A.; Paterno, L. G.; Kymissis, I. Organic thin-film transistors as gas sensors: A review. *Materials* **2021**, *14*, 3.

[14] Wang, C. L.; Dong, H. L.; Jiang, L.; Hu, W. P. Organic semiconductor crystals. *Chem. Soc. Rev.* **2018**, *47*, 422–500.

[15] Zhang, C. C.; Chen, P. L.; Hu, W. P. Organic field-effect transistor-based gas sensors. *Chem. Soc. Rev.* **2015**, *44*, 2087–2107.

[16] Wu, X. H.; Du, R. R.; Fang, L.; Chu, Y. L.; Li, Z.; Huang, J. Grain size adjustion in organic field-effect transistors for chemical sensing performance improvement. *Sci. China Mater.* **2019**, *62*, 138–145.

[17] Yu, S. H.; Cho, J.; Sim, K. M.; Ha, J. U.; Chung, D. S. Morphology-driven high-performance polymer transistor-based ammonia gas sensor. *ACS Appl. Mater. Interfaces* **2016**, *8*, 6570–6576.

[18] Peng, B. Y.; Huang, S. Y.; Zhou, Z. W.; Chan, P. K. L. Solution-processed monolayer organic crystals for high-performance field-effect transistors and ultrasensitive gas sensors. *Adv. Funct. Mater.* **2017**, *27*, 1700999.

[19] Kwak, D. H.; Seo, Y.; Anthony, J. E.; Kim, S.; Hur, J.; Chae, H.; Park, H. J.; Kim, B. G.; Lee, E.; Ko, S. et al. Enhanced gas sensing performance of organic field-effect transistors by modulating the

dimensions of triethylsilylethynyl-anthradithiophene microcrystal arrays. *Adv. Mater. Interfaces* **2020**, *7*, 1901696.
[20] Song, J.; Cui, X. Y.; Liu, P.; Shi, Y. H.; Wang, X. J.; Li, M.; Zhou, Y. Y.; Yang, J. E.; Liu, H. R.; Yan, Y. et al. Organic nanowire sensor with seeing, smelling and heat sensation capabilities. *Chem. Eng. J.* **2024**, *486*, 150378.
[21] Wang, Y.; Zhang, J. Y.; Zhang, S. Q.; Huang, J. OFET chemical sensors: Chemical sensors based on ultrathin organic field-effect transistors. *Polym. Int.* **2021**, *70*, 414–425.
[22] Xiao, Y. L.; Deng, W.; Hong, J. J.; Ren, X. B.; Zhang, X. J.; Shi, J. L.; Sheng, F. M.; Zhang, X. H.; Jie, J. S. Water-surface-mediated precise patterning of organic single-crystalline films via double-blade coating for high-performance organic transistors. *Adv. Funct. Mater.* **2023**, *33*, 2213788.
[23] Yuan, Y. B.; Giri, G.; Ayzner, A. L.; Zoombelt, A. P.; Mannsfeld, S. C. B.; Chen, J. H.; Nordlund, D.; Toney, M. F.; Huang, J. S.; Bao, Z. N. Ultra-high mobility transparent organic thin film transistors grown by an off-centre spin-coating method. *Nat. Commun.* **2014**, *5*, 3005.
[24] Yao, J. R.; Tian, X. Z.; Li, B.; Wang, Z. F.; Zhang, X. L.; Jie, J. S.; Yang, F. X.; Li, R. J.; Hu, W. P. Nonclassical growth of atomically flat two-dimensional organic single crystals on a liquid surface through fusion. *Adv. Electron. Mater.* **2023**, *9*, 2201027.
[25] Jeong, G.; Cheon, H. J.; Shin, S. Y.; Wi, E.; Kyokunzire, P.; Cheon, H.; Van Tran, V.; Vu, T. T.; Chang, M. Improved NO_2 gas sensing performance of nanoporous conjugated polymer (CP) thin films by incorporating preformed CP nanowires. *Dyes Pigm.* **2023**, *214*, 111235.
[26] Huang, L. Z.; Wang, Z.; Chen, J. H.; Wang, B. H.; Chen, Y.; Huang, W.; Chi, L. F.; Marks, T. J.; Facchetti, A. Porous semiconducting polymers enable high-performance electrochemical transistors. *Adv. Mater.* **2021**, *33*, 2007041.
[27] Zhang, X. N.; Wang, B. H.; Huang, L. Z.; Huang, W.; Wang, Z.; Zhu, W. G.; Chen, Y.; Mao, Y. L.; Facchetti, A.; Marks, T. J. Breath figure-derived porous semiconducting films for organic electronics. *Sci. Adv.* **2020**, *6*, eaaz1042.
[28] Lu, J. J.; Liu, D. P.; Zhou, J. C.; Chu, Y. L.; Chen, Y. T.; Wu, X. H.; Huang, J. Porous organic field-effect transistors for enhanced chemical sensing performances. *Adv. Funct. Mater.* **2017**, *27*, 1700018.
[29] Tran, V. V.; Jeong, G.; Wi, E.; Lee, D.; Chang, M. Design and fabrication of ultrathin nanoporous donor–acceptor copolymer-based organic field-effect transistors for enhanced VOC sensing performance. *ACS Appl. Mater. Interfaces* **2023**, *15*, 21270–21283.
[30] Chen, L.; Hu, Y. Z.; Huang, H. X.; Liu, C.; Wu, D.; Xia, J. L. Direct laser patterning of organic semiconductors for high performance OFET-based gas sensors. *J. Mater. Chem. C* **2023**, *11*, 7088–7097.
[31] Gao, L.; Liu, C. J.; Peng, Y. J.; Deng, J. Y.; Hou, S. H.; Cheng, Y. H.; Huang, W.; Yu, J. S. Ultrasensitive flexible NO_2 gas sensors via multilayer porous polymer film. *Sens. Actuators B: Chem.* **2022**, *368*, 132113.
[32] Li, H. Y.; Shi, Y. J.; Han, G. C.; Liu, J.; Zhang, J.; Li, C. L.; Liu, J.; Yi, Y. P.; Li, T.; Gao, X. K. et al. Monolayer two-dimensional molecular crystals for an ultrasensitive OFET-based chemical sensor. *Angew. Chem., Int. Ed.* **2020**, *59*, 4380–4384.
[33] Fu, B. B.; Yang, F. X.; Sun, L. J.; Zhao, Q.; Ji, D. Y.; Sun, Y. J.; Zhang, X. T.; Hu, W. P. Challenging bendable organic single crystal and transistor arrays with high mobility and durability toward flexible electronics. *Adv. Mater.* **2022**, *34*, 2203330.
[34] Zhang, Y. J.; Guo, Y.; Song, L.; Qian, J.; Jiang, S.; Wang, Q. J.; Wang, X. R.; Shi, Y.; Wang, X. M.; Li, Y. Directly writing 2D organic semiconducting crystals for high-performance field-effect transistors. *J. Mater. Chem. C* **2017**, *5*, 11246–11251.
[35] Jo, P. S.; Vailionis, A.; Park, Y. M.; Salleo, A. Scalable fabrication of strongly textured organic semiconductor micropatterns by capillary force lithography. *Adv. Mater.* **2012**, *24*, 3269–3274.
[36] Ye, X.; Liu, Y.; Han, Q. X.; Ge, C.; Cui, S. Y.; Zhang, L. L.; Zheng, X. X.; Liu, G. F.; Liu, J.; Liu, D. et al. Microspacing in-air sublimation growth of organic crystals. *Chem. Mater.* **2018**, *30*, 412–420.
[37] Lin, Q. L.; Ye, X.; Guo, Q.; Zheng, X. X.; Han, Q. X.; Zhang, L. L.; Cui, S. Y.; Li, C. C.; Jiang, J. K.; Liu, Y. et al. Fabrication of wafer-scale organic single-crystal films with uniform in-plane orientation via wetting-assisted in-air sublimation for high-performance transistor arrays. *Chem. Mater.* **2022**, *34*, 1030–1040.
[38] Lin, Q. L.; Ye, X.; Guo, Q.; Zheng, X. X.; Han, Q. X.; Li, C. C.; Jiang, J. K.; Liu, Y.; Tao, X. T. Homogeneously oriented organic single-crystalline patterns grown by microspacing in-air sublimation. *Small Methods* **2023**, *7*, 2201374.
[39] Schweicher, G.; Liu, G. F.; Fastré, P.; Resel, R.; Abbas, M.; Wantz, G.; Geerts, Y. H. Directional crystallization of C8-BTBT-C8 thin films in a temperature gradient. *Mater. Chem. Front.* **2021**, *5*, 249–258.
[40] Tsujita, K.; Maruyama, S.; Shibata, Y.; Koganezawa, T.; Kaminaga, K.; Fujikake, H.; Matsumoto, Y. Directional lateral crystallization of vacuum-deposited C8-BTBT thin films via liquid crystal phase by a seeded horizontal temperature gradient cooling technique. *CrystEngComm* **2023**, *25*, 64–71.
[41] Han, M. J.; Lee, D. W.; Lee, E. K.; Kim, J. Y.; Jung, J. Y.; Kang, H.; Ahn, H.; Shin, T. J.; Yoon, D. K.; Park, J. I. Molecular orientation control of liquid crystal organic semiconductor for high-performance organic field-effect transistors. *ACS Appl. Mater. Interfaces* **2021**, *13*, 11125–11133.
[42] Wang, W. C.; Zhong, D. Y.; Zhu, J.; Kalischewski, F.; Dou, R. F.; Wedeking, K.; Wang, Y.; Heuer, A.; Fuchs, H.; Erker, G. et al. Patterned nucleation control in vacuum deposition of organic molecules. *Phys. Rev. Lett.* **2007**, *98*, 225504.
[43] Yen, T. Y.; Hung, Y. H.; Lee, Y. Z.; Ho, Y. T.; Lan, Y. W.; Wu, C. H.; Hung, K. M.; Lo, K. Y. Gas adsorption mechanism on 2D materials: The hyperpolarizability evolution analyzed by nonlinear optics. *Adv. Funct. Mater.* **2024**, *34*, 2406005.
[44] Iqbal, H. F.; Waldrip, M.; Chen, H.; McCulloch, I.; Jurchescu, O. D. Elucidating the role of water-related traps in the operation of polymer field-effect transistors. *Adv. Electron. Mater.* **2021**, *7*, 2100393.
[45] Yin, Y.; Wang, X. P.; Xue, D.; Lu, J.; Zhang, Y. Y.; Gong, W. J.; Yan, C.; Wang, Z.; Wang, L.; Chi, L. F. et al. Bulk trapping organic semiconductor with amino-additive enabling ultrasensitive NO_2 sensors. *ACS Appl. Mater. Interfaces* **2024**, *16*, 23684–23694.
[46] Wang, Z.; Hu, J.; Lu, J.; Zhu, X. F.; Zhou, X.; Huang, L. Z.; Chi, L. F. Charge transport manipulation via interface doping: Achieving ultrasensitive organic semiconductor gas sensors. *ACS Appl. Mater. Interfaces* **2023**, *15*, 8355–8366.